ELSEVIER

Computational Materials Science 13 (1998) 90–102

COMPUTATIONAL MATERIALS SCIENCE

Micromechanics of creep fracture: simulation of intergranular crack growth

Patrick Onck *, Erik van der Giessen

Delft University of Technology, Koiter Institute Delft, Mekelweg 2, 2628 CD Delft, The Netherlands

Abstract

A computational model is presented to analyze intergranular creep crack growth in a polycrystalline aggregate in a discrete manner and based directly on the underlying physical micromechanisms. A crack tip process zone is used in which grains and their grain boundaries are represented discretely, while the surrounding undamaged material is described as a continuum. The constitutive description of the grain boundaries accounts for the relevant physical mechanisms, i.e. viscous grain boundary sliding, the nucleation and growth of grain boundary cavities, and microcracking by the coalescence of cavities. Discrete propagation of the main crack occurs by linking up of neighbouring facet microcracks. Assuming small-scale damage conditions, the model is used to simulate the initial stages of crack growth under C^* controlled, model I loading conditions. Initially sharp or blunted cracks are considered. The emphasis in this study is on the effect of the grain microstructure on crack growth.

1. Introduction

High temperature failure of polycrystalline metals (see [1] for an overview) spans a wide range of length scales, as illustrated in Fig. 1. At the largest, i.e. macroscopic, scale we consider a component or test specimen containing a crack (Fig. 1(a)), while the smallest relevant scale is that of the key failure mechanism, i.e. the nucleation and growth of small cavities along the grain boundaries (Fig. 1(e)). The intermediate scales determine how this elemental mechanism leads to growth of the macroscopic crack. At the second smallest length scale (Fig. 1(d)), we observe the individual grains in the material and the distribution of cavitation damage along its grain boundaries. This is also the scale where two other key mechanisms are operating, namely creep of the grains themselves and sliding of adjacent grains relative to each other. Coalescence of the cavities after sufficient growth leads to microcracks along the grain facets, and at the next larger length scale we are concerned with the distribution of these microcracks near the tip of the crack (Fig. 1(c)). Growth of the crack at this scale occurs by the linking-up of facet microcracks with the main crack. Zooming out further (Fig. 1(b)) brings us to the size scale at which we are no longer able to distinguish the grain microstructure of the material; what remains is that we can identify a zone in the neighbourhood of the crack tip in which damage occurs. This damage zone is surrounded by a zone of material that is not damaged and which only creeps (Fig. 1(b)).

* Corresponding author. Tel.: +31 15 278 27 03; fax: +31 15 278 21 50; e-mail: p.r.onck@wbmt.tudelft.nl

0927-0256/98/$ – see front matter
PII: S0927-0256(98)00049-4

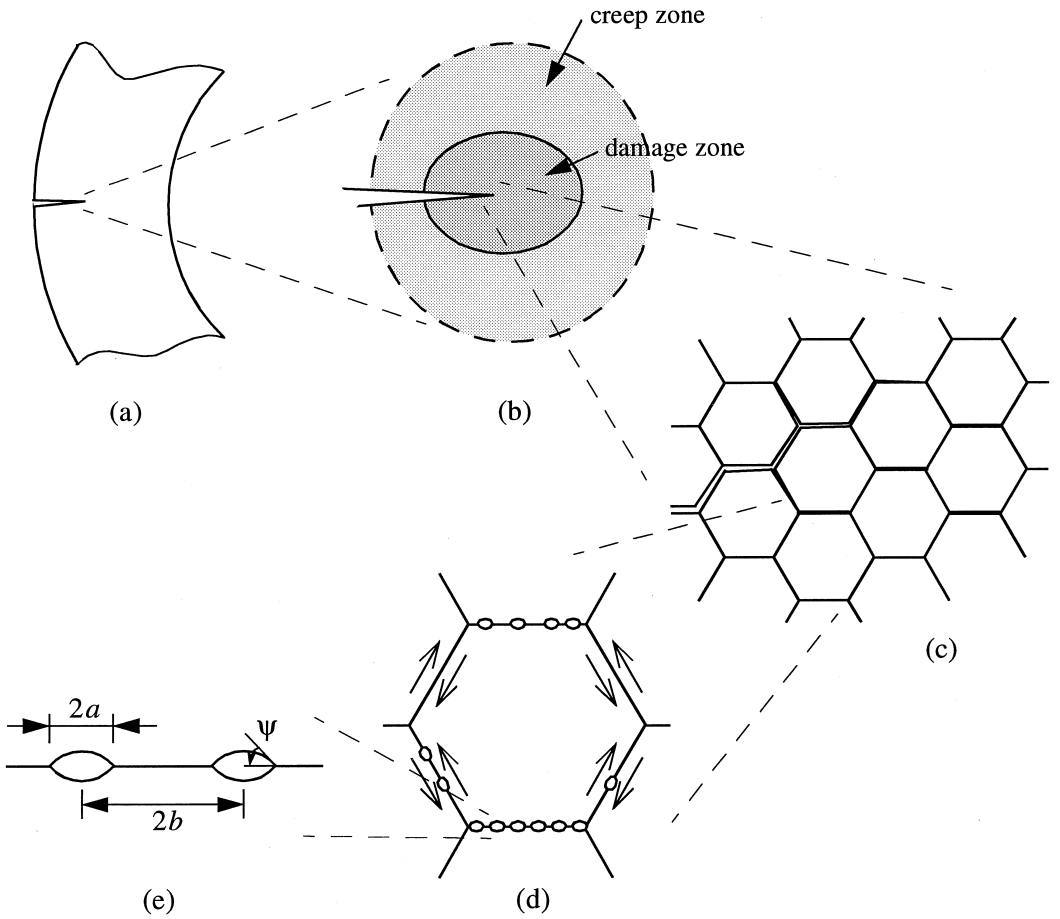

Fig. 1. Size scales involved in creep fracture: (a) macroscopic crack; (b) crack-tip neighbourhood with creep and damage zones; (c) mesoscopic near-tip region inside damage zone; (d) individual grains and grain boundary damage; (e) microscopic grain boundary cavities.

A thorough understanding of creep fracture requires that all relevant length scales are bridged. This poses an enormous challenge, since there are various competing mechanisms involved, each having its own characteristic time scale and dependence on stress and microstructure. Approaches in the literature now have either started from the macroscopic scale (Fig. 1(a) and (b)) or from the opposite microscopic scales (Fig. 1(d) and (e)). The more engineering, macroscopic approaches include nonlinear fracture mechanics approaches and continuum damage modelling (e.g. [2,3]). On the other hand, micromechanical studies have focussed on the basic damage processes of cavity growth (e.g. [4]) and grain boundary sliding (e.g. [5]), and their combination (e.g. [6]). The missing link is at the size scale depicted in Fig. 1(c).

The authors have recently proposed a computational procedure to forge this missing link [7,8]. The approach adopts a two-dimensional microstructural model of the material by individually representing a large number of grains surrounding the propagating crack. Cavitation and sliding along all grain boundaries in this aggregate is considered, and is described by a set of constitutive equations based on micromechanical studies at the smaller scales (Fig. 1(d) and (e)). The approach

allows to study the characteristics of the intergranular crack growth (e.g. crack growth rate as a function of loading) in a discrete manner and on the basis of the relevant mechanisms.

One of the features of this kind of model is that it allows to pick up the influence of the material's microstructure, i.e. the orientation and shape of all grains. Even though real materials usually contain a distribution of grain shapes and sizes, grains in two dimensions are often assumed to have a hexagonal shape and to be all identical. Random variations on such a regular structure are known to affect the creep [9] and damage processes [10], but for intergranular crack propagation also the orientations of the grains, or rather the grain facets, will have an effect. It is the objective of this paper to gain some insight into this effect using the methodology of [7,8]. We will do so by focusing on the initial stages of crack growth under mode I creep loading conditions. After presenting the exact problem and the microstructural models used (Section 2) and discussing the key ingredients for the computational method (Section 3), we discuss growth from an initially sharp crack (Section 5) and proceed with considering an initially blunted crack (Section 6).

2. Formulation

We consider a region near the tip of a pre-existing macroscopic crack that is subjected to mode I loading. We assume that it is contained well within the creep zone shown in Fig. 1(b) but is much larger than the damage zone, i.e. we consider small-scale damage conditions. Outside the damage zone, the material deforms elastically and by dislocation creep (Fig. 2(a)). Inside this region, it is appropriate to represent the polycrystalline material by a continuum giving a description averaged over many grains. Inside the anticipated damage zone or process zone (Fig. 2(b)), all grains making up the aggregate are represented individually. All grains are assumed to have the same hexagonal shape for simplicity, but we allow for two different orientations of the hexagonal microstructure. One of them is such that 1/3 of all grain facets are oriented parallel to the crack plane. The other microstructure is oriented perpendicular to the first. Both microstructures respect symmetry with respect to the initial crack plane, so that only half of the region needs to be analyzed. In either case, the process window consists of roughly 1600 grains for all results to be presented here.

Under steady-state conditions, the material sufficiently far away from the damage zone deforms by creep only. Assuming an isotropic response, the creep rate is given by the Norton power-law

$$\dot{\epsilon}_{\mathrm{e}}^{\mathrm{C}} = B\sigma_{\mathrm{e}}^{n}, \tag{1}$$

with B the creep parameter, n the creep exponent and σ_{e} the Mises stress. If the crack would be mathematically sharp, the stress field remote from the damage zone would coincide with the HRR field

$$\sigma^{ij} = \left[\frac{C^*}{BI_n r}\right]^{1/(n+1)} \tilde{\sigma}^{ij}(\theta, n), \tag{2}$$

with C^* the amplitude of the fields and with $\tilde{\sigma}^{ij}$ a nondimensional angular function and I_n a constant, both depending on n (r and θ are polar coordinates centered at the tip of the crack). For the cases analyzed here where the crack is initially sharp, we therefore use this field to determine the boundary conditions along the outer radius of the region as well as the initial conditions. When analyzing cases where the crack tip is initially blunted, the HRR field is employed for the boundary conditions. Clearly, since the HHR-field is only valid for a sharp crack, some time is needed before the stress field around the notch has converged to a steady-state solution. Only then damage development is allowed to occur.

3. Computational procedure

The problem outlined above is analyzed using an incremental, finite strain, finite element model involving two discretizations: one for the material inside the process zone and one outside this zone. Details of the procedure may be found in [7]; it suffices here to only reiterate the key ingredients.

The region in Fig. 2(a) outside the damage zone is described by a standard continuum and discretized with standard continuum finite elements.

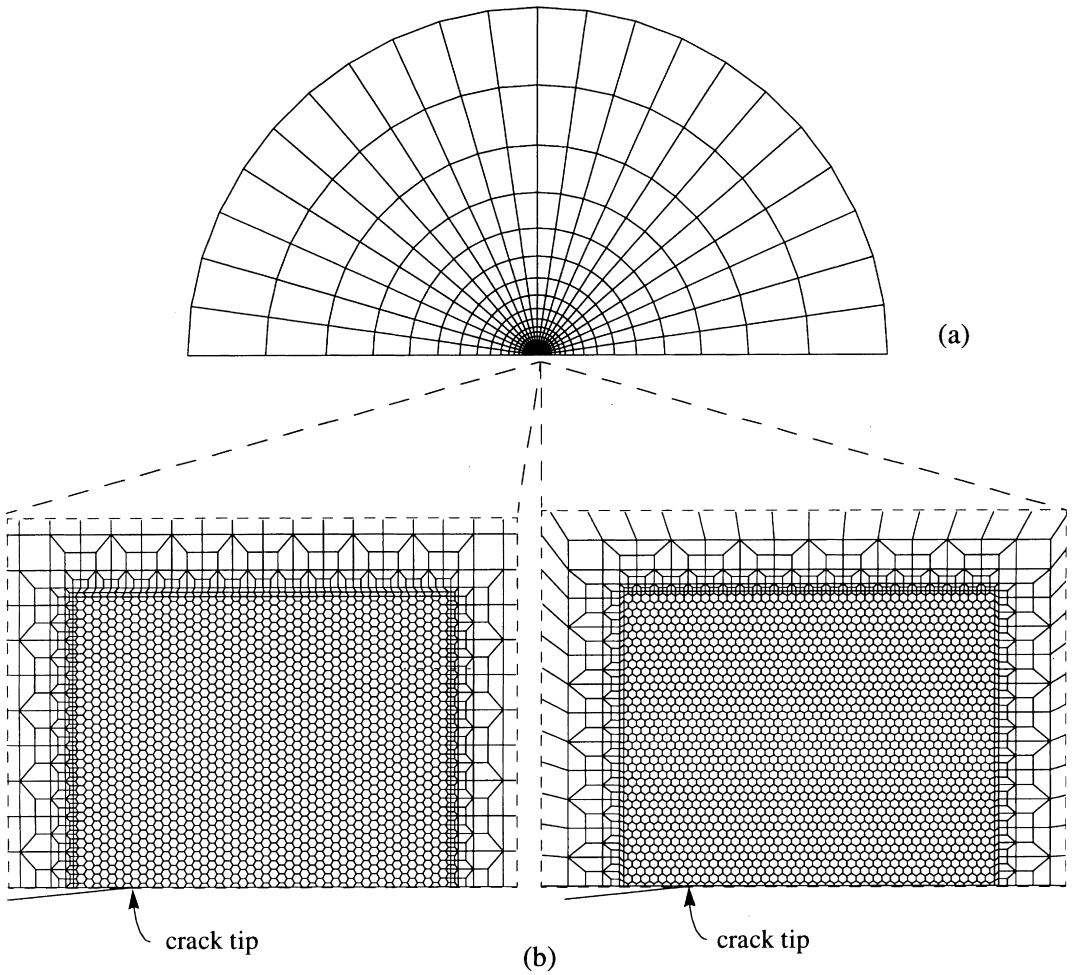

Fig. 2. The small-scale damage problem for an initially sharp crack subject to mode I loading. The outer region (a) deforms by elasticity and creep, and is modelled as a continuum. The damage zone (b) consists of an aggregate of approximately 1600 discrete hexagonal grains. Two principal orientations of the grains are considered.

The continuum constitutive equations are assumed to represent the average behaviour of an aggregate of grains. Hence, isotropic elasticity and dislocation creep are assumed. The elastic response is taken to be governed by the relationship

$$\overset{\nabla}{\boldsymbol{\sigma}} = \mathscr{R} : \boldsymbol{D}^{\mathrm{E}} = \mathscr{R} : (\boldsymbol{D} - \boldsymbol{D}^{\mathrm{C}}), \tag{3}$$

in terms of the well-known Jaumann rate of Cauchy stress, $\overset{\nabla}{\boldsymbol{\sigma}}$, and the elastic part of the stretching tensor $\boldsymbol{D}$. The fourth-order modulus tensor $\mathscr{R}$ is expressed in the usual way in terms of the Young's modulus E and Poisson's ratio v. The creep rate tensor $\boldsymbol{D}^{\mathrm{C}}$ in Eq. (3) is determined by the creep law Eq. (1) through the normality condition

$$\boldsymbol{D}^{\mathrm{C}} = \frac{3}{2}\dot{\epsilon}_{\mathrm{e}}^{\mathrm{C}}\frac{\boldsymbol{s}}{\sigma_{\mathrm{e}}}, \tag{4}$$

where $\boldsymbol{s}$ is the Cauchy stress deviator $\boldsymbol{\sigma}$ and $\sigma_{\mathrm{e}} = \sqrt{3\boldsymbol{s} : \boldsymbol{s}/2}$ is the effective Mises stress.

Each grain in the process zone is represented by a single, so-called grain element, while the grain boundary facets are treated by special-purpose interface elements. The grain elements used here are, in effect, super-elements with six nodes per

element, while the interface elements consist of two nodes [11]. Each grain element accounts for the elastic and creep behaviour of an individual grain. Obviously, the creep behaviour of individual grains is anisotropic. Incorporating this would introduce a stochastic effect, which would obscure the interpretation of the fracture process. Therefore, as in [4,6,10,15], we neglect any grain anisotropy, so that the constitutive equations for the grain material are also of the form Eq. (3).

The grain-boundary elements are designed to incorporate the relevant mechanisms that take place inside the grain boundaries, i.e. grain boundary sliding and grain boundary cavitation. The set of constitutive equations that govern these mechanisms are phrased, as is usual in interface formulations, in terms of the displacement jumps across the interface as a function, primarily, of the conjugate tractions. Grain boundary sliding is expressed through the following viscous relationship jump in tangential displacement rate, $\dot{u}_s$, as suggested by Ashby [12]:

$$\dot{u}_s = w\frac{\tau}{\eta_B}. \tag{5}$$

Here, τ is the shear stress in the grain boundary, w its thickness and η_B the grain boundary viscosity. The cavitation process along the boundary govern the grain boundary behaviour in the normal direction through the normal jump in displacement, δ_c, in function of the facet normal stress σ_n. The displacement jump is identical to the average separation between grains, as determined by the average volume of the grain boundary cavities, V, and their spacing b: $\delta_c = V/(\pi b^2)$ [13]. Thus, the rate of change

$$\dot{\delta}_c = \frac{\dot{V}}{\pi b^2} - \frac{2V}{\pi b^2}\frac{\dot{b}}{b} \tag{6}$$

is determined by the volumetric growth rate $\dot{V}$ of the cavities, and by the rate of change of the cavity spacing $\dot{b}$.

Ignoring finite strain effects for the sake of clarity, the cavity spacing changes in the course of the failure process due to the nucleation of new cavities, i.e.

$$\frac{\dot{b}}{b} = \frac{1}{2}\frac{\dot{N}}{N}, \tag{7}$$

with N the cavity density. Cavity nucleation is the least understood mechanism of creep fracture and convincing, physically-based nucleation models appear to be largely lacking till today. As discussed in ample detail in [7], we therefore resort to a phenomenological description. Nucleation is taken to be driven by the facet normal stress σ_n and by the local creep rate $\dot{\epsilon}_e^C$, such that, once nucleation occurs, it proceeds with a rate given by

$$\dot{N} = F_n(\sigma_n/\Sigma_0)^2\dot{\epsilon}_e^C \quad \text{for } \sigma_n > 0, \tag{8}$$

until the density reaches a saturation value N_{max}. Here, Σ_0 is a normalization parameter and F_n is the nucleation activity parameter. However, before nucleation can start, the parameter

$$S = (\sigma_n/\Sigma_0)^2\epsilon_e^C \tag{9}$$

must have attained a threshold value S_{thr}, which is taken to be specified as $S_{thr} = N_I/F_n$ in terms of the cavity density N_I at the onset of nucleation.

The volumetric growth rate in Eq. (6) is due to the growth of the cavities by simultaneous grain boundary diffusion and creep. Detailed numerical studies of this phenomenon (at the size scale of Fig. 1(e)) have been carried out by Needleman and Rice [4] and by Sham and Needleman [14]. They also showed that their numerical results for the volumetric growth rate could be captured well by the expression (slightly modified in [15])

$$\dot{V} = \dot{V}_1 + \dot{V}_2, \tag{10}$$

where $\dot{V}_1$ is the contribution of diffusion, specified through

$$\dot{V}_1 = 4\pi\mathscr{D}\frac{\sigma_n - (1-f)\sigma_s}{\ln(1/f) - \frac{1}{2}(3-f)(1-f)} \tag{11}$$

with

$$f = \max\left[\left(\frac{a}{b}\right)^2, \left(\frac{a}{a+1.5L}\right)^2\right], \tag{12}$$

and where the contribution of creep, $\dot{V}_2$, is given by

$$\dot{V}_2 = \begin{cases} \pm 2\pi\dot{\epsilon}_e^C a^3 h(\psi)\left[\alpha_n\left|\frac{\sigma_m}{\sigma_e}\right| + \beta_n\right]^n, & \text{for } \pm\frac{\sigma_m}{\sigma_e} > 1, \\ 2\pi\dot{\epsilon}_e^C a^3 h(\psi)[\alpha_n + \beta_n]^n\frac{\sigma_m}{\sigma_e} & \text{for } \left|\frac{\sigma_m}{\sigma_e}\right| \leqslant 1. \end{cases} \tag{13}$$

Here (see Fig. 1(e)), a is the current cavity radius, $2b$ their spacing and h incorporates the assumed

spherical-caps shape of the cavities as a function of their tip angle ψ : $h(\psi) = [(1+\cos\psi)^{-1} - \frac{1}{2}\cos\psi]/\sin\psi$ (we use $\psi = 75°$). The sintering stress σ_s in Eq. (11) is usually relatively small and will be neglected; $\mathscr{D}$ is the grain boundary diffusion parameter. The constants α_n and β_n in Eq. (13) are given by $\alpha_n = 3/(2n)$ and $\beta_n = (n-1)(n+0.4319)/n^2$. The coupling between diffusion and creep enters in the definition of f in Eq. (12) through the length parameter [4]

$$L = \left[\mathscr{D}\sigma_e/\dot{\epsilon}_e^C\right]^{1/3}. \tag{14}$$

For small values of a/L (say, $a/L < 0.1$) cavity growth is dominated by diffusion, while for larger values of a/L creep growth becomes more and more important. Just as in the stress dependence of cavity nucleation, the effective stress σ_e, the mean stress σ_m and the normal stress σ_n in Eqs. (11)–(14) are stresses remote from each cavity on the size scale of individual cavities, but are local quantities on the scale of grains. In the computation, their values are inferred from the two adjacent grains.

The final constitutive relationship for the grain boundary in normal direction is obtained by substitution of Eqs. (7), (8), (10)–(14) into Eq. (6). During the computation, Eqs. (7) and (10) are integrated to give the current cavity spacing b and volume V, while the latter is used at each instant to compute the instantaneous cavity radius a from $V = 4/3\pi a^3 h(\psi)$. When the ratio a/b approaches unity, coalescence of cavities occurs; here, we use $a/b = 0.7$ to signal coalescence. Once this has occurred, the grain boundary facet has lost its stress-carrying capacity and the interface element represents a facet microcrack.

4. Parameters

As we shall present all results in nondimensional form, all parameters that govern the problem will also be specified nondimensionally. All lengths are scaled with the initial half-width of the grain facets, R_I, while cavity densities are normalized by $N_R = 1/(\pi R_I^2)$. Stresses are normalized with the reference stress Σ which is taken to be the magnitude of the HRR stress field at a distance R_I from the tip: $\Sigma = (C^*/BI_nR_I)^{1/(n+1)}$. The reference time $t_R = 1/\dot{E}_e^C$, based on $\dot{E}_e^C = B\Sigma^n$, is used to normalize time.

All cases to be presented have used $n = 5$ and $\nu = 0.3$, and are for a crack loading C^* specified through $\Sigma/E = 0.9\times10^{-3}$, so that elastic deformations remain small. The grain boundary viscosity η_B in Eq. (5) is specified in terms of the ratio $\dot{E}_e^C/\dot{\epsilon}_B$, with [5]

$$\dot{\epsilon}_B = \left(\frac{w}{d}\frac{B^{-1/n}}{\eta_B}\right)^{n/(n-1)},$$

d being the effective grain size, $d = 3.64R_I$. Free sliding ($\eta_B = 0$) corresponds to $\dot{E}_e^C/\dot{\epsilon}_B = 0$, while no sliding ($\eta_B \to \infty$) is equivalent to $\dot{E}_e^C/\dot{\epsilon}_B \to \infty$; here, we have used $\dot{E}_e^C/\dot{\epsilon}_B = 10$. Free sliding is discussed in [7].

The density and size of freshly nucleated cavities is taken according to $N_I/N_R = 40$ and $a_I/R_I = 0.67\times10^{-3}$, respectively, while $N_{max} = 100N_R$ in all cases (other values are considered in [8]). The two main parameters that govern nucleation and diffusive growth are F_n and $\mathscr{D}$ (Σ_0 in Eq. (8) is arbitrarily chosen equal to Σ), and they are specified in terms of F_n/N_R and L_R/R_I, respectively, with L_R defined as $L_R = (\mathscr{D}\Sigma/\dot{E}_e^C)^{1/3}$. As explained in detail in [7], a relatively large value of L_R/R_I implies that cavity growth occurs predominantly by diffusion, with creep strains remaining small so as to lead to 'brittle' fracture. As L_R/R_I decreases, creep deformations increase (while cavity growth may still be diffusion dominated) and fracture becomes more 'ductile'. Parallel to this distinction, Dyson [16] pointed out that there is a tendency at larger values of L_R/R_I that diffusive cavity growth is being constrained by creep of the surrounding grains. In the present study, we employ two sets of parameters that will be shown to lead to rather brittle ($L_R/R_I = 0.1$) or more ductile ($L_R/R_I = 0.032$) behaviour. The value of the nucleation activity F_n is taken to be coupled to that of $\mathscr{D}$ so that the maximum density N_{max} is approximately reached at the moment of cavity coalescence. This leads to $F_n/N_R = 2.4\times10^3$ and $F_n/N_R = 5.3\times10^4$ for the ductile and brittle case, respectively. Finally, it is noted that the material is considered to be homogeneous in that all grains and grain facets

in the process window have the same material properties.

5. Initially sharp crack

We start by studying crack growth of an initially sharp crack (as illustrated in Fig. 2) in the two different microstructures. Fig. 3 demonstrates the development of cavitation damage in the two microstructures for material and loading conditions such that $L_R/R_I = 0.032$. The cavitation state is shown by plotting the value of a/b perpendicular to each facet and with the ordinate along the facet. Evidently, damage initiates from the crack tip as soon as S according to Eq. (9) reaches the threshold value for cavity nucleation. With increasing time, the damage zone further expands by continuous cavity nucleation, while the damage inside this zone intensifies due to cavity growth, until coalescence leads to facet microcracks (indicated by black shading). Especially in the second

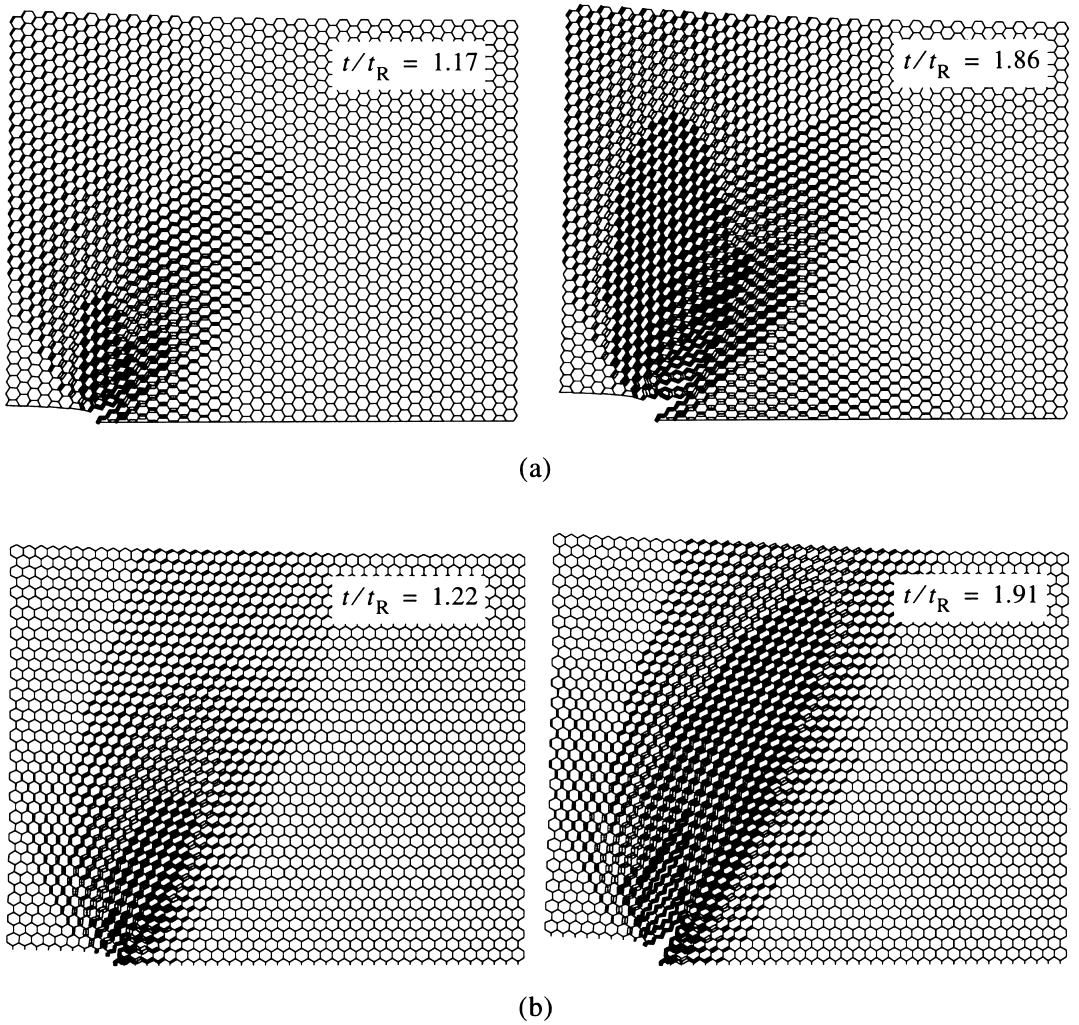

Fig. 3. Snapshots of the damage distribution at two instants during crack growth from the initially sharp crack for each of the two microstructures (a) vs. (b) with $L_R/R_I = 0.032$. Values of a/b are plotted along and on either side of the facets. Microcracked facets, where $a/b = 0.7$, are highlighted in black.

stage shown, it is clear that the first microstructure in Fig. 3(a) develops two families of like-oriented microcracks: one above the original crack tip with microcracks along facets with a normal of $-30°$ with respect to the original crack direction, and a second one which comprises transverse facets. Extension of the macroscopic crack requires the linking-up of microcracks. Grain boundary sliding is one possible mechanism, but the viscosity in these calculations is apparently so high that it is more favourable that microcracking occurs on adjacent facets in the region where the two families of microcracks overlap. This leads to short strings of microcracks roughly along a 30° direction with the crack plane, with the macrocrack actually propagating by the joining of these strings of microcracks along a direction of around 60°.

In the second microstructure (Fig. 3(b)), damage is again seen to develop mainly on two out of three families of grain facets, but they are not concentrated so clearly in two distinct regions. Microcracks thus develop along facets with normals at $-60°$ and along facets parallel to the loading direction. Linking-up of these microcracks now occurs in the 60° direction and the macrocrack propagates in roughly the same direction as in the other microstructure or at a slightly larger angle.

Fig. 4 shows the damage distribution developing in the two microstructures when $L_R/R_I = 0.1$, i.e. when diffusion is more important. Comparing the crack tip openings with those in Fig. 3 confirms that the present value of L_R/R_I corresponds to considerably more brittle creep fracture. In both microstructures, advance of the macroscopic cracks occurs by linking-up of the same two families of microcracks as identified before for the more ductile case in Fig. 3, but the progressive formation of strings of linked-up microcracks is not necessarily the same. For the second microstructure (Fig. 4(b)), this leads to a crack growth direction that appears to be very close to that in Fig. 3(b), but for the first one (Fig. 4(a)), the crack seems to advance at a somewhat lower angle.

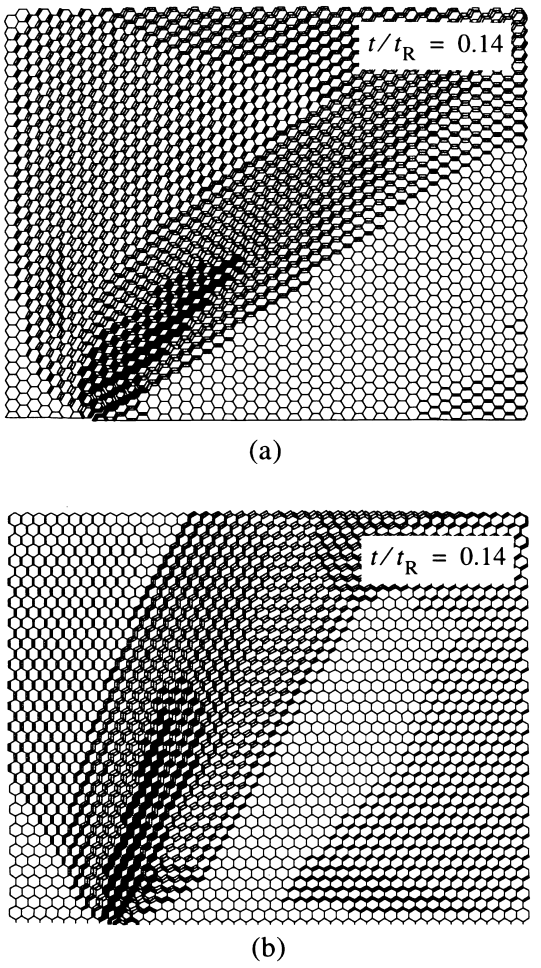

Fig. 4. Snapshot of the damage distribution during crack growth from the initially sharp crack for each of the two microstructures (a) vs. (b) with $L_R/R_I = 0.1$.

6. Blunted crack

The initial stress state corresponding to steady-state creep around blunt cracks is obviously distinctly different from that near mathematically sharp cracks. We consider the consequences of this for initially blunted cracks with a tip radius of $12\sqrt{3}R_I$ ($\sim 5.7d$).

Typical damage states after some crack growth for $L_R/R_I = 0.032$ are shown in Fig. 5. As compared to the damage patterns for the sharp crack cases in Fig. 3, there is much more damage development right ahead of the crack. Especially microcracking of the transverse facets in Fig. 5(a) concentrates more strongly in front of the crack, and so do the $-60°$ microcracks in the microstructure of Fig. 5(b). However, there are still two

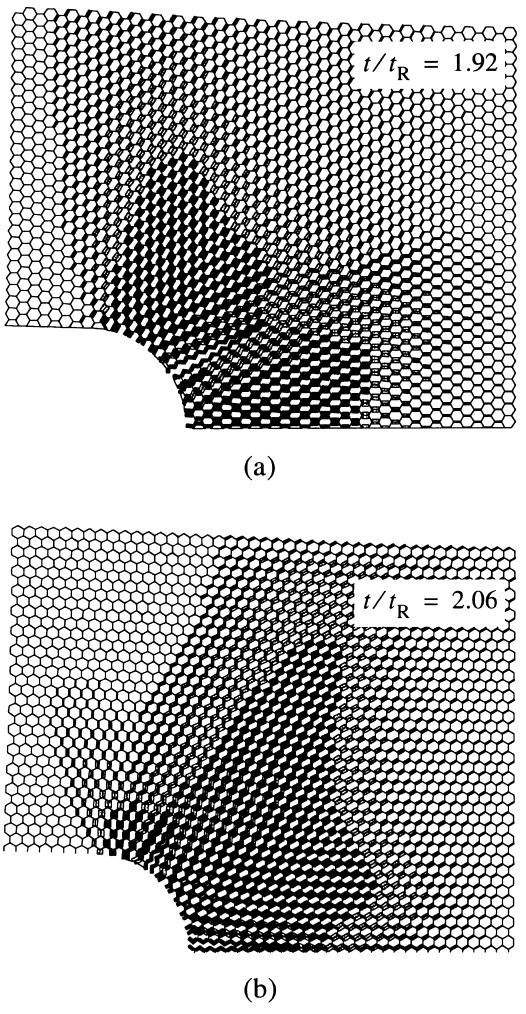

Fig. 5. Snapshot of the damage distribution during crack growth from the initially blunted crack for each of the two microstructures (a) vs. (b) with $L_R/R_I = 0.032$.

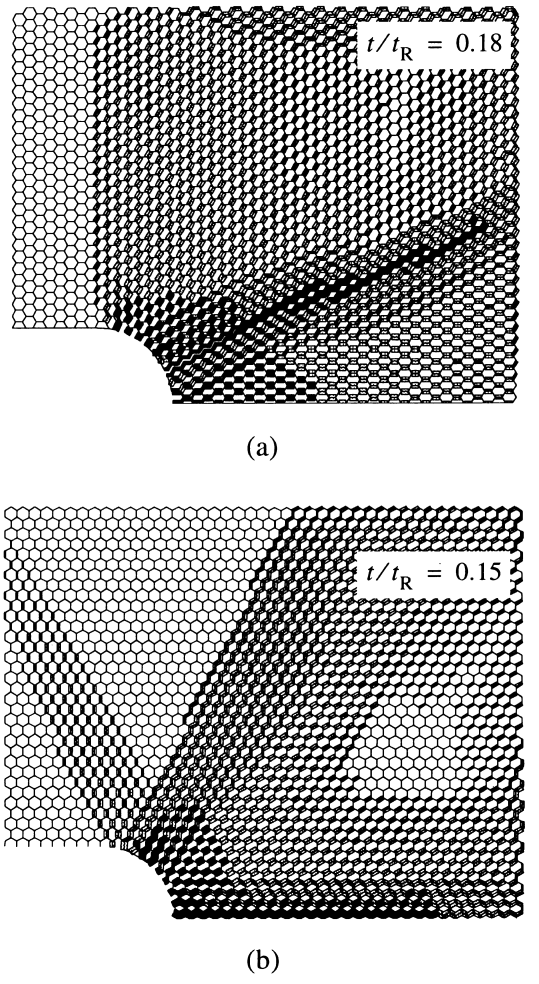

Fig. 6. Snapshot of the damage distribution during crack growth from the initially blunted crack for each of the two microstructures (a) vs. (b) with $L_R/R_I = 0.1$.

families of microcracks and actual crack extension still occurs by linking-up in the regions where the two families intersect. For the first microstructure this appears to be in a direction of 30°, while for the second microstructure two cracks emanate. The one along the crack plane appears to grow most rapidly.

Repeating the calculations with $L_R/R_I = 0.1$ leads again to more brittle fracture, as seen in Fig. 6. For both microstructures the regions of intense microcracking are now considerably smaller than in Fig. 5. Crack growth in the microstructure of Fig. 6(a) occurs in the same, approximately 30° direction as in Fig. 5(a), while in the second microstructure the crack tends to remain on the crack plane.

7. Discussion

After having considered the effect of microstructure on the crack growth direction in the previous sections, we now address the possible effect on crack growth rate. Fig. 7 summarizes the

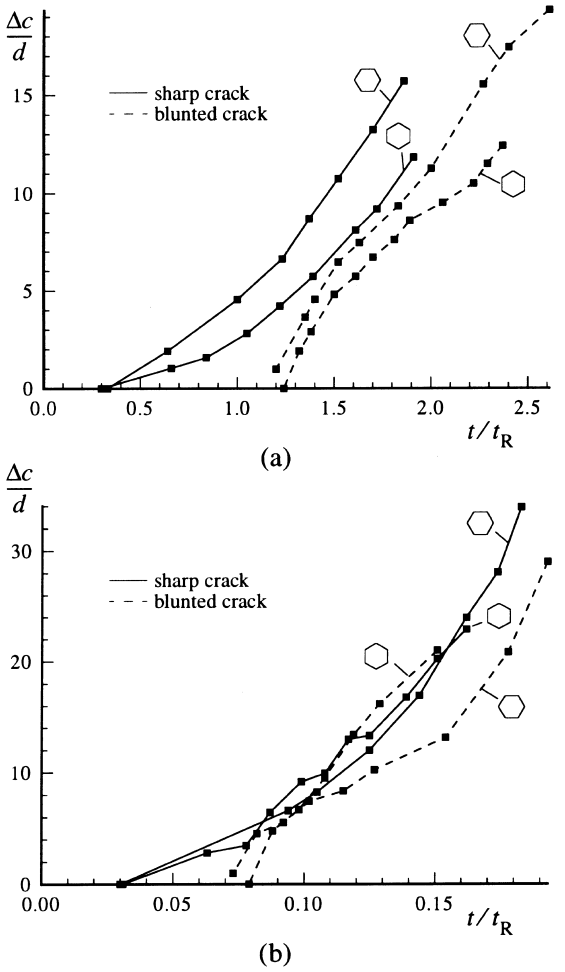

Fig. 7. Crack extension Δc, normalized by the grain size d, in the two microstructures for (a) the 'ductile' cases, $L_R/R_I = 0.032$ (cf. Figs. 3 and 5), and (b) the 'brittle' cases, $L_R/R_I = 0.1$ (cf. Figs. 4 and 6).

crack propagation inferred from the various cases presented above. In view of the distributed microcracking that develops, there is not a unique current crack tip; as a working definition, the crack extension Δc plotted in Fig. 7 is taken to be the distance to the tip of the most distant string of microcracks (the current 'crack tip'). It is seen that the two microstructures analyzed lead to grossly the same crack growth response for the same set of parameters, especially for those corresponding to the brittle behaviour (Fig. 7(b)). The incubation times before crack growth actually starts appear to be independent of the microstructure, both for the sharp and for the blunt crack. Also, the average crack growth rates after a transient period are fairly close for both microstructures. In fact, it seems from Fig. 7 that these ultimate values are the same for the initially sharp as well as for the blunted crack. However, the amount of crack extension must be considered to be too small for steady-state growth to be attained.

Detailed evaluation of the numerical results reveals that the stress fields in the 'brittle' cases ($L_R/R_I = 0.1$) presented above drastically change once damage develops. This is caused by the creep constraint on cavity growth which requires load shedding away from the damaged regions [16]. By contrast, the stress fields for the 'ductile' cases ($L_R/R_I = 0.032$) remain roughly the same as the original steady-state creep fields, even close to the microcracked tip region. In view of this, we can rationalize the directions of damage and microcracking on the basis of the initial fields.

Fig. 8 illustrates the angular distributions of the facet normal stresses in the initial steady-state creep state for viscous sliding conditions ($\dot{E}_e^C/\dot{\epsilon}_B = 10$) around a sharp crack for both microstructures. The normal stresses on individual facets, it will be recalled from Eq. (11), is the main driving force for diffusive cavity growth, and for the computations discussed here this is the most dominant growth mechanism. Creep deformations are an essential contribution to cavity nucleation, cf. (8). For the sharp crack they are distributed according to the well-known HRR field, with the maximum value almost right above the crack tip. Careful examination of the numerical results reveals that the latter is responsible for the highly damaged regions seen in Fig. 3 right above the initial crack tip. The region of concentrated damage on transverse facets in Fig. 3(a) ($\theta < 60°$ or so) can be traced back to the fact that the normal stresses on these facets are highest in this region (Fig. 8(a)). Normal stresses on the $-60°$ facets in the second morphology attain peak values between 50° and 80°, which is indeed the region where intense microcracking on these facets occurred (Fig. 3(b)).

The difference in these stress distributions with the distribution of facet normal stresses according to the initial steady-state creep fields around the

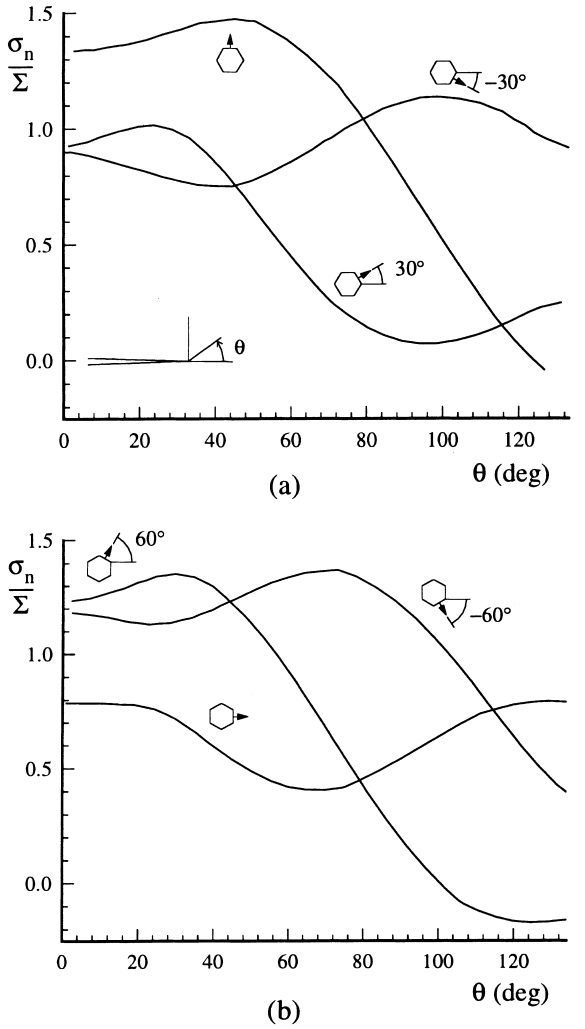

Fig. 8. Angular distribution of the initial normal facet stresses at the three grain boundary facet orientations for each of the two microstructures (a) vs. (b) at $r = 10d$ for the initially sharp crack.

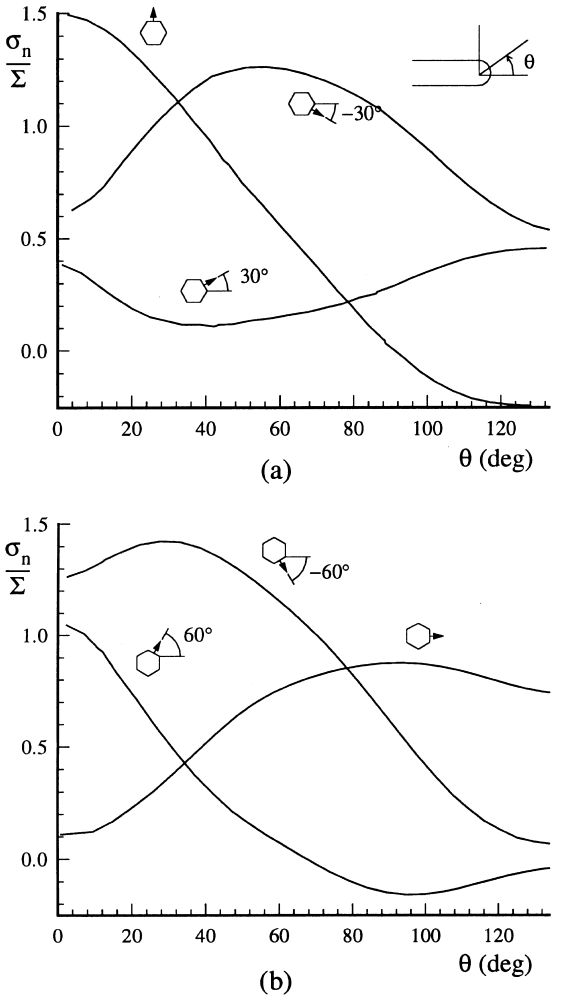

Fig. 9. Angular distribution of the initial normal facet stresses at the three grain boundary facet orientations for each of the two microstructures (a) vs. (b) at $r = 10d$ for the blunt crack.

blunt notch, shown in Fig. 9, can likewise help to rationalize the difference in crack growth behaviour between Figs. 3 and 5. First, we see that the peak in normal stress on transverse facets in the first microstructure is shifted from around 45° for the sharp crack (Fig. 8) to around 0° for the blunted tip (Fig. 9). A similar tendency is observed for the −60° facets in the second morphology, and both observations are consistent with the damage concentrating more in front of the crack (Fig. 5). Secondly, we find that the directions where the facet stresses on the two controlling families of facets are equal have decreased from around 80° and 110° for the two microstructures with the sharp crack (see Fig. 8) to around 30° and 80° according to Fig. 9 for the blunt crack. This equality ensures roughly equal times to coalescence on the two facets, which is favourable for linking-up. Indeed, the latter two directions agree quite well with the crack growth directions found in the simulations in Fig. 5. Fig. 9(b) also shows that normal stresses on −60° and 60° facets are

almost equal at $\theta \approx 0^\circ$, which explains the microcrack linking-up process right in front of the crack in Fig. 5(b).

These simple considerations do not apply to the 'brittle' cases considered in Figs. 4 and 6 because of the continuous stress re-distribution that takes place in order to accommodate the creep constrained cavitation processes. The stress re-distributions tend to favour cavitation in front of the crack, but this only leads to mild deviations in the crack growth directions compared to those in the 'ductile' cases that we investigated. This can be readily observed when comparing the results in Fig. 4 with Fig. 3 and Fig. 6 with Fig. 5.

8. Conclusion

By virtue of the fact that grains in a region around a crack are represented in a discrete manner, the model allows to address the influence of the granular microstructure on creep crack growth. In this paper, we have focussed on the effect of orientations of grain boundary facets in order to gain an understanding of the importance of assuming a particular microstructural orientation. It is important to note that we have only considered the morphological effects of grain orientations. The associated crystallographic orientations inside the grains may also have an effect through the anisotropy of creep properties. These effects have not been considered, but can be incorporated in principle. One of the difficulties, however, is that the results will necessarily contain a certain stochastic nature associated with the crystallographic grain orientations.

This is not the only extension which involves stochastic variations in properties. It is also pertinent to perform simulations, for example, (i) where grain boundary properties concerning cavity nucleation and grain boundary diffusion vary among the grain facets, and/or (ii) where grains vary in size and shape, resulting in a random variation of facet size and orientation. Random variations of the nucleation activity parameter F_n in Eq. (8) have been explored in [7,8], and it was found, for instance, that these variations did not significantly alter the predicted crack growth directions in the assumed grain structure. At this stage, it is an open question how random variations of the size and orientation of grain facets will influence the crack growth process, including the crack growth direction. Based on the findings in previous work [7,8] and this, we expect that within the framework of a symmetrized model as used here (Fig. 2), the average crack growth direction over many grains will be roughly in the range spanned by the directions found for the two periodic microstructures. However, a more realistic investigation of this effect requires a model of the complete process window rather than just the half, symmetric window. Presumably, this type of an analysis will predict meandering of the growing crack over many grain distances, which may be controlled to a small extent by the randomness in microstructure, but more importantly by the continuously evolving stress fields.

References

[1] H. Riedel, Fracture at High Temperatures, Springer, Berlin, 1987.
[2] D.R. Hayhurst, P.R. Brown, C.J. Morrison, The role of continuum damage in creep crack growth, Phil. Trans. Roy. Soc. A311 (1984) 131–158.
[3] V. Tvergaard, Analysis of creep crack growth by grain boundary cavitation, Int. J. Fracture 31 (1986) 183–209.
[4] A. Needleman, J.R. Rice, Plastic creep flow effects in the diffusive cavitation of grain boundaries, Acta Metall. 28 (1980) 1315–1332.
[5] F. Ghahremani, Effect of grain boundary sliding on steady creep of polycrystals, Int. J. Solids Struc. 16 (1980) 847–862.
[6] E. Van der Giessen, V. Tvergaard, A creep rupture model accounting for cavitation at sliding grain boundaries, Int. J. Fracture 48 (1991) 153–178.
[7] P.R. Onck, E. Van der Giessen, Growth of an initially-sharp crack by grain-boundary cavitation, J. Mech. Phys. Solids (1998), in press.
[8] P.R. Onck, E. Van der Giessen, Microstructural modelling of creep crack growth from a blunted crack, J. Fracture (1998), in press.
[9] P.R. Onck, E. Van der Giessen, Influence of microstructural variations on steady state creep and facet stresses in 2-D freely sliding polycrystals, Int. J. Solids Struct. 34 (1997) 703–726.
[10] E. Van der Giessen, V. Tvergaard, Effect of random variations in microstructure on the development of final creep failure in polycrystalline aggregates, Model. Simul. Mater. Sci. Eng. 2 (1994) 721–738.

[11] P.R. Onck, E. Van der Giessen, Microstructurally-based modelling of intergranular creep fracture using grain-elements, Mech. Mater. 26 (1997) 109–126.
[12] M.F. Ashby, Boundary defects and atomistic aspects of boundary sliding and diffusional creep, Surf. Sci. 31 (1972) 498–542.
[13] J.R. Rice, Constraints on the diffusive cavitation of isolated grain boundary facets in creeping polycrystals, Acta Metall. 29 (1981) 675–681.
[14] T.-L. Sham, A. Needleman, Effects of triaxial stressing on creep cavitation of grain boundaries, Acta Metall. 31 (1983) 919–926.
[15] V. Tvergaard, On the creep constrained diffusive cavitation of grain boundary facets, J. Mech. Phys. Solids 32 (1984) 373–393.
[16] B.F. Dyson, Constraints on diffusional cavity growth rates, Metal Sci. 10 (1976) 349–353.